

# Spectrally constrained chromophore and scattering near-infrared tomography provides quantitative and robust reconstruction

Subhadra Srinivasan, Brian W. Pogue, Shudong Jiang, Hamid Dehghani, and Keith D. Paulsen

A multispectral direct chromophore and scattering reconstruction technique has been implemented for near-infrared frequency-domain tomography in recovering images of total hemoglobin, oxygen saturation, water, and scatter parameters. The method applies the spectral constraint of the chromophores and scattering spectra directly in the reconstruction algorithm, thereby reducing the parameter space of the inversion process. This new method was validated by use of simulated and experimental data, and results show better robustness and stability in the presence of higher levels of noise. The method suppresses artifacts, especially those significant in water and scatter power images, and reduces cross talk between chromophore and scatter parameters. Variation in scattering was followed by this spectral approach successfully in experimental data from 90-mm-diameter cylindrical phantoms, and results show linear variation in scatter amplitude and reduced scattering coefficient ( $\mu_s'$ ), with total hemoglobin, oxygen saturation, and water remaining constant and quantitatively accurate. Similar experiments were carried out for varying oxygen saturation and total hemoglobin. Accurate quantification was obtained with a mean error of 7.7% for oxygen saturation and 6.2% for total hemoglobin, with minimal cross talk between different parameters. © 2005 Optical Society of America

OCIS codes: 170.3010, 170.6960.

## 1. Introduction

Near-infrared (NIR) tomography can be used to characterize malignant and normal tissue based on the high-contrast available from heme in the blood, leading to images that are related to intrinsic pathophysiologic processes such as angiogenesis and hypoxia. Absorption-based parameters can be recovered such as total hemoglobin in the tissue, hemoglobin oxygen saturation, and water fraction. It is also possible to estimate elastic scattering images that may provide information about the composition of the tissue. *In vivo* studies have demonstrated levels of hemoglobin in tumors over twice that in normal breast,<sup>1,2</sup> and lower levels of oxygen saturation have been found in malignancies<sup>2,3</sup>; however, one of the current chal-

lenges is to optimize the quantitative accuracy with which these parameters can be determined. The quantification of chromophores and scattering parameters relies upon the spectral decomposition of the images acquired at a sparse number of discrete wavelengths instead of a complete spectrum. This sparse spectral sampling coupled with an image reconstruction process that is ill posed, tends to amplify errors in quantifying the spatially resolved parameters of the tissue. In this study a spectrally constrained approach to image reconstruction is introduced, which follows the recent pioneering developments proposed by Corlu *et al.*<sup>4</sup> and Li *et al.*,<sup>5</sup> who showed that incorporation of spectral information into the reconstruction process improves the uniqueness of the image formation by using continuous-wave data. In this paper the addition of phase information and the improved accuracy in fitting water and scattering power are specifically examined by use of this spectrally constrained approach. The improvement in quantification of water and scattering has dramatic implications in terms of the value of these particular parameters in breast imaging. The potential to reduce cross talk between chromophores is also important.

---

The authors are with the Department of Biomedical Engineering, Thayer School of Engineering, Dartmouth College, P.O. Box 8000, Hanover, New Hampshire 03755. S. Srinivasan's e-mail address is subha@dartmouth.edu.

Received 27 August 2004; revised manuscript received 22 November 2004; accepted 5 December 2004.

0003-6935/05/101858-12\$15.00/0

© 2005 Optical Society of America

In earlier research the absorption and scattering coefficients were recovered from boundary measurements of amplitude or phase or both on the object of interest, such as the breast or brain, by means of computational models in which both analytical and numerical approaches were used by different research groups.<sup>6–8</sup> After recovery of these optical coefficients, a spectral fitting to known absorption signatures of oxyhemoglobin, deoxyhemoglobin, and water is used to obtain the concentrations of these absorbing chromophores. Similarly, the reduced scattering coefficients at separate wavelengths were fit to yield the scatter amplitude ( $a$ ) and scatter power ( $b$ ), which are related to the structure of the tissue in terms of scatterer size and density. In this paper a modified reconstruction approach is used, which implements the possible spectral shapes of the chromophore and scattering models into the image formation process, thereby adding a spectral constraint into the reconstruction. The chromophore concentrations and scatter parameters are estimated directly by incorporating the known Beer's law attenuation relation and Mie scattering behavior as constraints. This type of parameter reduction has been applied in electrical impedance tomography in which Brandstatter *et al.*<sup>9</sup> showed that by using multifrequency data and by assuming a frequency dependence, one can reduce the ill-posed nature of the problem and make the reconstruction more robust to noise in data. A similar application in microwave image reconstruction<sup>10</sup> provides evidence of reduced artifacts in the images as a result of coupling measurements from different frequencies. Corlu *et al.*<sup>4</sup> implemented this approach by using continuous-wave (cw) measurements to find the optimal four wavelengths that reduce the cross talk between absorption and scatter parameters. Their results from simulations are encouraging and are based on the assumption that all change in scattering is due to the scatter amplitude with the scatter power kept constant. A similar approach to cw data has been implemented by Li *et al.*<sup>5</sup> used two of three wavelengths under the assumption that there is no scattering perturbation. They have applied this method to find chromophore concentrations directly and have shown in simulated and experimental data that their technique results in reduced image artifacts and parameter cross talk.

In the current study this overall approach is extended to the application of frequency-domain data, using six wavelengths. The method is evaluated with experimental data following individual variation of oxygen saturation, hemoglobin, and scattering parameters. A finite-element model of the diffusion equation is used, and the algorithm reconstructs images for five parameters: oxyhemoglobin, deoxyhemoglobin, water fraction, scatter amplitude, and scatter power, with no assumptions on the scatter amplitude or power. The results show that the new technique is more robust to noise in measurements than the conventional method. In addition, the spectral constraint reduces the noise in the recovered chromophore con-

centrations, especially in the water and scattering images, and the reconstructions from the experimental data show quantitatively accurate results.

## 2. Materials and Methods

### A. Instrumentation

The NIR frequency-domain system for breast imaging has been described in detail in previous papers.<sup>11</sup> Briefly, it consists of optical fibers placed in three planes in a circular geometry. Each plane has 16 source–detector positions, and intensity light modulated at 100 MHz is used at six different wavelengths in the range 660–850 nm. The signals are detected by high-gain photomultiplier tubes, and the electrical signals are passed through rf mixer circuits to heterodyne down to a 500-Hz offset frequency. The signal amplitude and phase are calibrated to compensate for system offsets by matching measured data from homogeneous phantoms<sup>12</sup> to simulated results from the finite-element model. When optimized, the calibrated data have less than 1% offset from simulated values and provide a highly stable data set from which to reconstruct absorption and scattering coefficient images.

### B. Reconstruction without Spectral Constraints

Under the assumption that breast tissue is a scatter-dominated medium, the diffusion approximation to the radiative transfer equation<sup>8,13</sup> was used to model the propagation of light at large distances from the source location. This is given by

$$-\nabla \cdot \kappa(r) \nabla \Phi(r, \omega) + \left( \mu_a(r) + \frac{i\omega}{c} \right) \Phi(r, \omega) = q_0(r, \omega), \quad (1)$$

where  $\Phi(r, \omega)$  is the isotropic fluence at modulation frequency  $\omega$  and position  $r$ ,  $\kappa(r)$  is the diffusion coefficient,  $\mu_a(r)$  is the absorption coefficient,  $c$  is the speed of light in the medium, and  $q_0(r, \omega)$  is an isotropic source. The diffusion coefficient can be written as

$$\kappa(r) = \frac{1}{3[\mu_a(r) + \mu_s'(r)]}, \quad (2)$$

where  $\mu_s'$  is the reduced scattering coefficient.

A finite-element-based-model solution to this equation was developed and was described and validated in Refs. 14 and 15. Briefly, the forward problem involves solving Eq. (1) for fluence, given an initial distribution of the optical properties, with the appropriate boundary conditions applied. The image reconstruction uses a Newton–Raphson minimization that iteratively updates the optical property parameters based on a least-squares-error norm given by

$$\chi^2 = \sum_i \left[ \frac{(\phi_i^{\text{meas}} - \phi_i^{\text{cal}})^2}{\sigma_i^2} \right], \quad (3)$$

where  $\phi_i^{\text{meas}}$  is the measured data and  $\phi_i^{\text{cal}}$  is the data calculated for an initial distribution of the properties, using the forward solver. Here the measurements are assumed to be independent of each other. Using a Taylor's series approximation for the solution at some close distance from the boundary data ( $\phi^{\text{cal}}$ ) for the initial distribution and ignoring the higher-order terms, the update in the optical properties is related to the difference between the measured and the calculated data as

$$\partial\phi = \mathfrak{J} \partial\mu, \quad (4)$$

where  $\partial\phi$  refers to the change in boundary data;  $\mathfrak{J}$  is the Jacobian, the matrix containing the sensitivity of the boundary data to a change in optical properties,  $\mathfrak{J} = [\mathfrak{J}_{\mu_a}; \mathfrak{J}_{\kappa}]$ ; and  $\partial\mu$  is the update in the optical properties given by  $\partial\mu = [\partial\mu_a; \partial\kappa]$ .

The reconstruction is sensitive to the initial estimate of the parameters, which are given by a homogeneous prefitting algorithm based on the analytical solution for infinite medium.<sup>12</sup> The matrix  $\mathfrak{J}$ , being ill conditioned, requires that the inverse problem in Eq. (4) be solved with the application of a Levenberg–Marquardt regularization scheme<sup>16,17</sup> for stabilization. The stopping criterion for this reconstruction was chosen to be when the  $\chi^2$  error in Eq. (3), known as the projection error, changes by less than 2% between successive iterations.

Previously<sup>18</sup> the optical properties at each wavelength were obtained, and then the calculation of the chromophore concentrations was performed with a constrained least-squares fit to the Beer's law relation

$$\mu_a = [\varepsilon]c, \quad (5)$$

where  $\varepsilon$  is the molar absorption spectra of the absorbing chromophores and  $c$  is the concentration of these chromophores. Oxyhemoglobin ( $\text{HbO}_2$ ), deoxyhemoglobin (Hb), and water are assumed to be the main absorbers, and their molar absorption spectra were obtained experimentally in our instrument. This approach of using values estimated by the system compensates for any offsets from the theoretical values, yet there was little difference between our experimental and theoretical estimates of molar absorption coefficients. By fitting for the concentrations, we calculate total hemoglobin as  $\text{HbT} = \text{HbO}_2 + \text{Hb}$  [in micromolar ( $\mu\text{M}$ )] and oxygen saturation as  $\text{SO}_2 = \text{HbO}_2/\text{HbT} \times 100$  (in percent); the contribution from other chromophores such as lipids has been found to be negligible, because the wavelengths used here were limited to less than 850 nm where lipid is a weak absorber. The constraints on the fitting process were for HbT to be below 100  $\mu\text{M}$ , oxygen saturation to be nonnegative and with an upper bound of 100%, and water to be in the range [0%, 100%].

Similarly, the  $\mu_s'$  spectrum of tissue has been shown to fit well to an empirical approximation to Mie scattering theory,<sup>19,20</sup> given by

$$\mu_s' = a\lambda^{-b}. \quad (6)$$

Equation (6) was used to derive the scatter amplitude (a) and the scatter power (b), with wavelength in micrometers. The coefficient  $\mu_s'$  has units of inverse millimeters, and  $b$  is dimensionless so that  $a$  has units given by  $10^{-3b}(\text{mm})^{b-1}$ . Both the scattering power and the amplitude depend on the scattering center size and number density and may reflect variations in breast structural composition due to different cellular, organelle, and structural sizes and densities for fatty and glandular tissue. Typically, large scatterers have lower  $b$  and  $a$  values, whereas small scatterers have higher  $b$  and  $a$  coefficients.<sup>19,20</sup> Although scatterers in tissue are not necessarily homogeneous spheres, as assumed in Eq. (6), studies on red blood cells and yeast have shown this to be a reasonable approximation since measurements of  $\mu_s'$  in these cells show trends similar to Mie theory.<sup>21,22</sup>

### C. Spectrally Constrained Chromophore and Scattering Reconstruction

Instead of estimating the optical properties at each wavelength and then spectrally deconvolving the chromophore concentrations [Eqs. (5) and (6)], one can incorporate these constraints into the reconstruction to directly determine oxyhemoglobin, deoxyhemoglobin, water, scatter amplitude, and scatter power, thus reducing the parameter space from 12 images ( $\mu_a$  and  $\mu_s'$  at 6 wavelengths) to 5 parametric images. Assuming that we know  $\mathfrak{J}_{\mu} = \partial\phi/\partial\mu$  and  $\mathfrak{J}_{\kappa} = \partial\phi/\partial\kappa$ , as calculated by the previous method (reconstruction without spectral priors), in the new approach the measurements at all wavelengths are coupled together, and the relations in Eqs. (5) and (6) are combined to create a new set of relations, which for each wavelength is represented by

$$\partial\phi_{\lambda} = \mathfrak{J}_{c,\lambda} \partial c + \mathfrak{J}_{a,\lambda} \partial a + \mathfrak{J}_{b,\lambda} \partial b, \quad (7)$$

where

$$\mathfrak{J}_{c,\lambda} = \frac{\partial\phi}{\partial c} \Big|_{\lambda} = \frac{\partial\phi}{\partial\mu} \frac{\partial\mu}{\partial c} \Big|_{\lambda},$$

for each chromophore ( $c$ ) in the model. From Eq. (5) we get  $\partial\mu = \varepsilon\partial c$ , so that, substituting for  $\partial\mu/\partial c$ ,

$$\begin{aligned} \mathfrak{J}_{c,\lambda} &= \frac{\partial\phi}{\partial c} \Big|_{\lambda} = \frac{\partial\phi}{\partial\mu} \varepsilon \Big|_{\lambda} \\ &= \left( \frac{\partial\phi}{\partial\mu} \Big|_{\mu} \right) \otimes (\varepsilon_{\lambda}^{c1, c2, c3}) = \mathfrak{J}_{\mu, \lambda} \otimes (\varepsilon_{\lambda}^{c1, c2, c3}), \end{aligned} \quad (8)$$

where  $\otimes$  refers to the Kronecker tensor product.

Similarly,

$$\mathfrak{J}_{a,\lambda} = \frac{\partial\phi}{\partial a} \Big|_{\lambda} = \frac{\partial\phi}{\partial\kappa} \frac{\partial\kappa}{\partial a} \Big|_{\lambda}. \quad (9)$$

Rewriting

$$\frac{\partial \kappa}{\partial a} = \left( \frac{\partial \kappa}{\partial \mu_s'} \right) \left( \frac{\partial \mu_s'}{\partial a} \right)$$

and knowing that

$$\kappa = \frac{1}{3(\mu_a + \mu_s')},$$

we get

$$\frac{\partial \kappa}{\partial \mu_s'} = \frac{1}{3} \left[ \frac{-1}{(\mu_a + \mu_s')^2} \right] = \frac{1}{3} (-9\kappa^2) = -3\kappa^2,$$

$$\frac{\partial \mu_s'}{\partial a} = \lambda^{-b}.$$

Substituting these expressions in Eq. (9) leads to

$$\mathfrak{J}_{a,\lambda} = \frac{\partial \phi}{\partial a} = \frac{\partial \phi}{\partial \kappa} \frac{\partial \kappa}{\partial a} \Big|_{\lambda} = \mathfrak{J}_{\kappa} (-3\kappa^2)(\lambda^{-b}) \Big|_{\lambda}. \quad (10)$$

Similarly, for the scatter power

$$\begin{aligned} \mathfrak{J}_{b,\lambda} &= \frac{\partial \phi}{\partial b} = \frac{\partial \phi}{\partial \kappa} \frac{\partial \kappa}{\partial b} \Big|_{\lambda} \\ &= \left( \frac{\partial \phi}{\partial \kappa} \right) \left( \frac{\partial \kappa}{\partial \mu_s'} \right) \left( \frac{\partial \mu_s'}{\partial \ln \mu_s'} \right) \left( \frac{\partial \ln \mu_s'}{\partial b} \right). \end{aligned} \quad (11)$$

Knowing that  $\partial \ln \mu_s' = (1/\mu_s') \partial \mu_s' \Rightarrow \partial \mu_s' / \partial \ln \mu_s' = \mu_s'$  and from Eq. (6),  $\ln \mu_s' = \ln a - b \ln \lambda$ , then it is found that  $\partial \ln \mu_s' / \partial b = -\ln \lambda$ . Substituting these relations produces

$$\mathfrak{J}_{b,\lambda} = \mathfrak{J}_{\kappa} (-3\kappa^2)(\mu_s')(-\ln \lambda) \Big|_{\lambda}. \quad (12)$$

The overall system of equations is assembled by substituting the relations from Eqs. (8), (10), and (12) into Eq. (7):

$$\begin{pmatrix} \partial \phi_{\lambda 1} \\ \partial \phi_{\lambda 2} \\ \dots \\ \partial \phi_{\lambda n} \end{pmatrix} = \begin{bmatrix} \mathfrak{J}_{c1,\lambda 1} \mathfrak{J}_{c2,\lambda 1} \mathfrak{J}_{c3,\lambda 1} \mathfrak{J}_{a,\lambda 1} \mathfrak{J}_{b,\lambda 1} \\ \mathfrak{J}_{c1,\lambda 2} \mathfrak{J}_{c2,\lambda 2} \mathfrak{J}_{c3,\lambda 2} \mathfrak{J}_{a,\lambda 2} \mathfrak{J}_{b,\lambda 2} \\ \dots \\ \mathfrak{J}_{c1,\lambda n} \mathfrak{J}_{c2,\lambda n} \mathfrak{J}_{c3,\lambda n} \mathfrak{J}_{a,\lambda n} \mathfrak{J}_{b,\lambda n} \end{bmatrix} \begin{pmatrix} \partial c_1 \\ \partial c_2 \\ \partial c_3 \\ \partial a \\ \partial b \end{pmatrix}. \quad (13)$$

The size of the left-hand vector is equal to the number of wavelengths multiplied by the number of measurements per wavelength, and the size of the right-hand side vector is equal to the number of chromophores and scatter parameters multiplied by the number of nodes for updating each parameter in the mesh. The individual Jacobian matrices for each chromophore were computed with a dual-mesh technique,<sup>23</sup> on a 2000-node mesh for forward diffusion calculations and a 425-node mesh was used for image reconstruc-

tion. Equation (13) was implemented by building the new Jacobian ( $5 \times 425$  by  $480 \times 6$ ), and the same Levenberg–Marquardt regularization scheme was applied. The computation time was approximately 25 min for typically 5–7 iterations, with the measure of convergence being when the projection error was less than 2% of the previous iteration value. Additional constraints based on the physiologically possible values for the parameters were applied at each iteration so that HbT does not exceed 100  $\mu\text{M}$  (based on typical concentrations found in the breast), that oxygen saturation is in the range [0%, 100%], and that water is in the range [0%, 100%]. The scatter amplitude is bounded in the range [0.5, 2.0] in units of  $10^{-3b}(\text{mm})^{b-1}$ , and the scatter power is in the range [0, 2] based on previous studies,<sup>24</sup> so that together they cover the possible range for the reduced scattering coefficient. This range is [0.5, 3.25]  $\text{mm}^{-1}$  for 785 nm. The approach can easily be extended to additional wavelengths without any computational expense in the inversion process since the size of the new Hessian from Eq. (13) depends on the number of nodes and not on the number of measurements, although the number of wavelengths will influence the calculation of individual Jacobian matrices. The algorithm typically converges after a lower number of iterations than the conventional method does, and no spatial filtering was necessary since the noise in the images is already damped by the spectral constraints.

### 3. Results

Subsections 3.A and 3.B show the improvement of the spectral technique over the conventional method by quantitative assessment of the mean and standard deviation from recovered images by use of simulated and experimental data. The results shown in Subsections 3.C, 3.D, and 3.E focus on validating the accuracy of the spectral technique in following the variation of scattering, oxygen saturation (Hill curve), and total hemoglobin individually by use of the appropriate experiments.

#### A. Effect of Noise in Amplitude and Phase Measurements

It is expected that the spectrally constrained nature of this new algorithm will make the reconstruction more immune to noise in measurements as compared with the conventional method, since all data are coupled. More noise in the data is typically observed at 661 nm for tissues containing lower oxygenation (due to high absorption of deoxyhemoglobin) and 849 nm (due to water absorption) and in higher-scattering cases. This behavior is taken into consideration in the algorithm by the *a priori* spectral information. To test the hypothesis of reduced noise sensitivity of the spectral method, we simulated amplitude and phase data at six wavelengths by using the finite-element model for a homogeneous phantom of diameter 86 mm with concentrations of 30  $\mu\text{M}$  HbO<sub>2</sub>, 30- $\mu\text{M}$  Hb, 60% water, scatter amplitude of 1 [units of  $10^{-3b}(\text{mm})^{b-1}$ ], and scatter power of 1. This yields

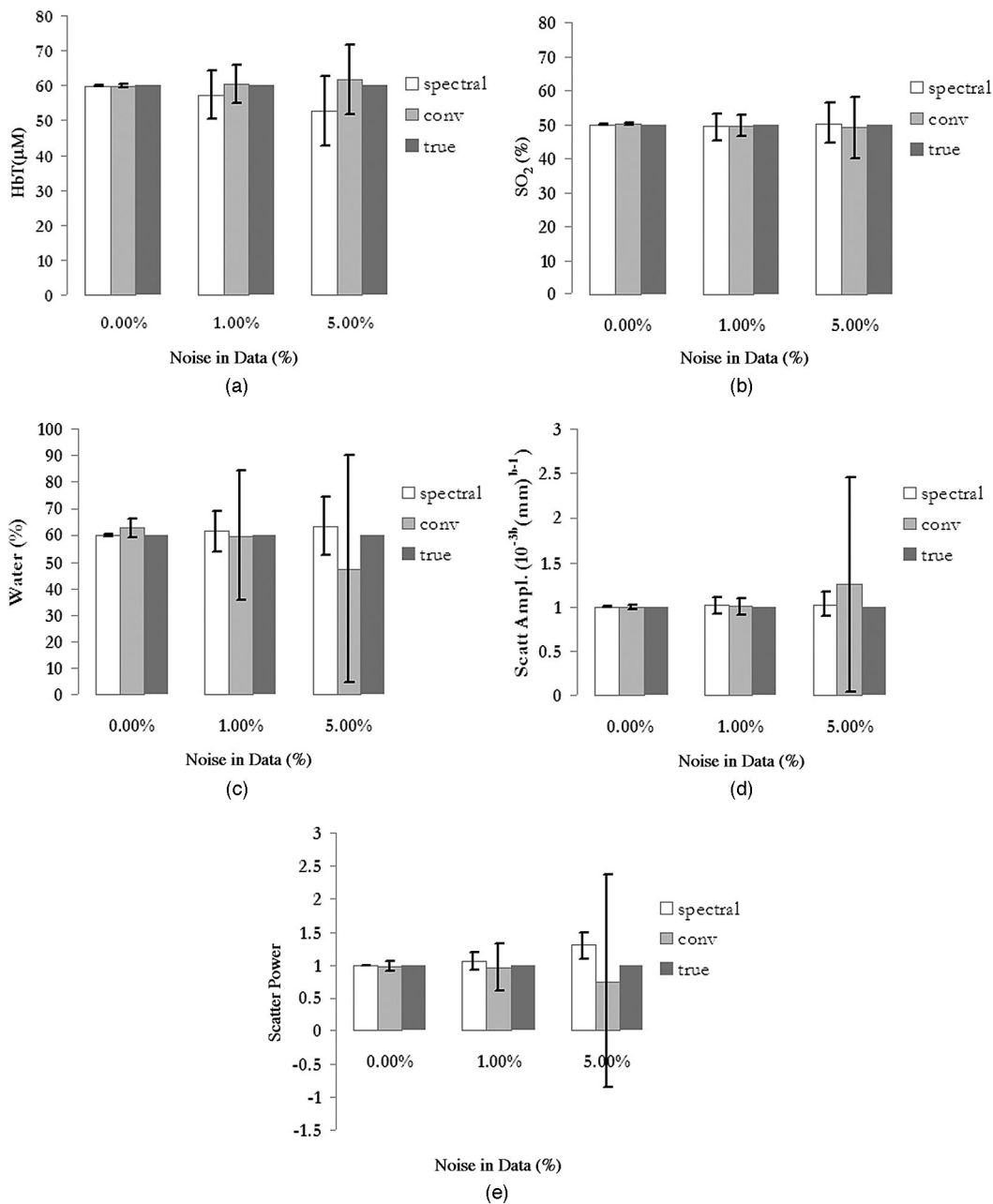


Fig. 1. Recovered mean values with standard deviation error bars are shown for (a) hemoglobin, (b) oxygen saturation ( $\text{SO}_2$ ), (c) water (in percent), (d) scatter amplitude, and (e) scatter power. These were estimated from the interior of a homogeneous field reconstructed with different levels of noise in the original data. Values for the new spectrally constrained reconstruction are shown alongside results from the conventional approach.

total hemoglobin of  $60 \mu\text{M}$ ,  $\text{SO}_2 = 50\%$ , and  $\mu_s'$  at  $785 \text{ nm} = 1.27 \text{ mm}^{-1}$ , which are concentrations typically found in the breast. Random Gaussian distributed noise was added to the amplitude and phase measurements in a systematic manner from 0.5% to 5%, and the spectrally constrained reconstruction was carried out on the data. The conventional technique of reconstructing each wavelength separately and then carrying out the spectral fit was also applied to these data for comparison. The mean and standard deviation for the reconstructed images from both techniques for each of the parameters are plotted in

Fig. 1; the results are shown for the cases with no noise, 1% noise, and 5% noise.

For the noiseless data reconstruction, both techniques show an accurate recovery of all five parameters (mean is within 3% of the true value), with an average standard deviation of 0.5% of the mean for the spectral method and 3.7% for the conventional technique. For the 1% and 5% noise cases, the standard deviation increases as expected; however, this increase is much more evident in the images from the conventional technique than from the spectral method. The results from the spectral method do not

differ significantly from the conventional technique for total hemoglobin and oxygen saturation images; however, the noise is significantly suppressed in the water and scatter images from the spectral method. For 1% noise in data, the mean is still within 5% of the true value for both methods, but the standard deviation in water has reduced from 40% in the conventional method to 12% of the mean for the spectral technique. Even in the 5% noise case, the spectral method shows a reasonable recovery of mean values for the parameters (accurate to within 10% on an average), with a 15.3% standard deviation (as percent of the mean). This shows a reduced sensitivity of the reconstruction to higher levels of noise compared with the conventional method.

#### B. Reduced Standard Deviation in Homogeneous Experimental Data

To assess the mean and standard deviation from homogeneous images in experimental data, we collected measurements on a liquid tissue-simulating phantom within a plastic circular container of 90-mm diameter, consisting of 9.3- $\mu\text{M}$  pig blood in buffered saline and 1% Intralipid concentration. The blood hematocrit was measured before the experiment with a clinical co-oximeter that showed 1% of the pig blood contained 9.3  $\mu\text{M}$  of hemoglobin for this sample. The expected values for the scatter amplitude and scatter power were derived from the work of van Staveren *et al.*<sup>19</sup> Using the expression given by van Staveren *et al.* with the units suitably modified produces the following equation:  $\mu_s' = 0.928\lambda^{-1.4} - 0.16\lambda^{-2.4}$ . Incorporating the higher-order term into the scatter amplitude factor (since the amplitude factor of the second term is much lower than that of the first term) by assuming that  $\mu_s' = 1 \text{ mm}^{-1}$  at 800 nm, the scatter amplitude ( $a$ ) = 0.73 and the scatter power ( $b$ ) = 1.4. Water and oxygen saturation are expected to be close to 100%, since the phantom was an oxygenated liquid solution. Both the spectral and conventional techniques were applied to this data, and the mean and standard deviation from the reconstructed images are plotted in Fig. 2(a), along with the expected values. As described in Section 2, both reconstructions were terminated by use of the projection error criterion, and reconstructed parameters 15 mm from the edge have been removed from the calculation of mean and standard deviation to diminish contribution from any boundary artifacts.

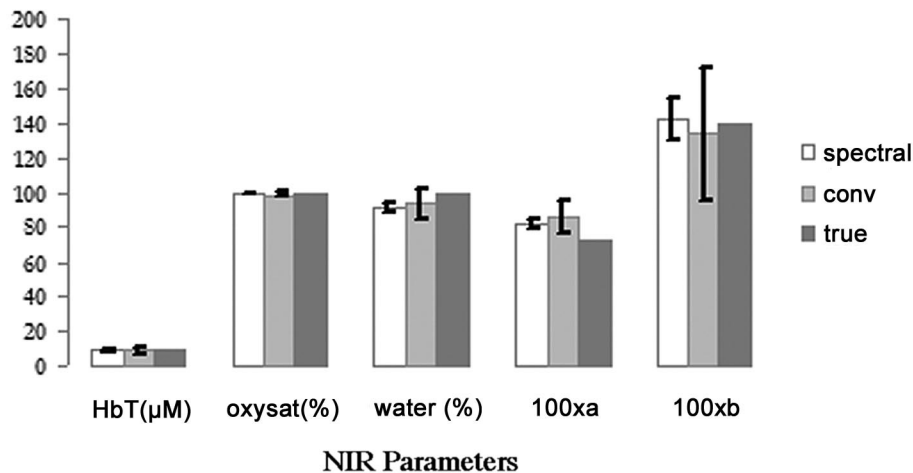
Figure 2(a) shows the reduced standard deviation in the images obtained from the spectral method, compared with the conventional technique. The mean values for the parameters are accurate to within 6%, on average, for the spectral scheme and to within 11% for the conventional method. As with the simulations, no spatial filtering is applied to the spectral reconstruction, whereas the conventional method uses a mean filter. The stopping criterion for the spectral technique is a projection error change of less than 2% between iterations, and it converges in seven iterations. For the conventional method, the equivalent 7th iteration at

every wavelength was used to obtain images based on earlier studies<sup>25</sup> that indicated 5–9 iterations are most suitable for experimental data. Both methods use the same initial regularization parameter (equal to 10 in this study<sup>15</sup>). The main improvement here was the suppression of noise in the water and scattering images by use of the spectral technique.

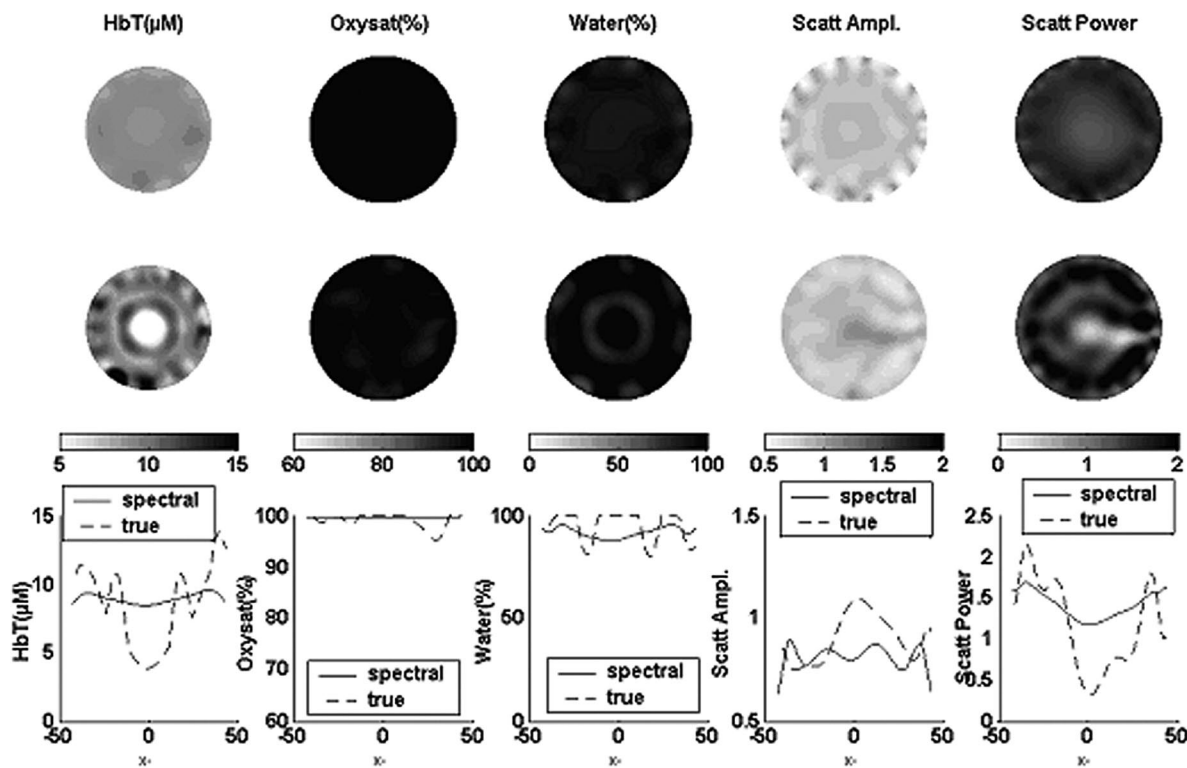
Figure 2(b) shows the reconstructed images from both methods along with a cross section of the middle plane. The spatial variation in the cross section is less in the spectral technique, and some of the boundary artifacts in the hemoglobin, water, and scatter power images are reduced. The scatter amplitude image shows some artifacts close to the boundary, which may indicate the need for higher regularization for the parameter. The hemoglobin and water images from the conventional technique show some cross talk between the images. A central artifact can be seen in the HbT image in which there is a decrease in its value, with saturation in the water image at this same region (=100%). The scatter parameter images, especially scatter power, show considerable noise that is possibly due to cross talk between the two scatter parameters and between deoxyhemoglobin and scatter.

#### C. Scattering Parameter Validation

Having shown that spectral reconstruction is superior to the conventional method of reconstructing each wavelength separately and then applying the spectral information in terms of reduced sensitivity to noise in the data and suppression of artifacts in the images, we now focus the following sections on validating the accuracy of the spectral reconstruction. One of the key advantages of the spectral method over the conventional technique is the reduction of noise in the water and scatter parameters. The implementation of this technique on frequency-domain measurements allows the separation of absorption and scatter, and this along with multiwavelength capability allows a modest separation of the scatter amplitude and scatter power. To test the cross talk and noise in the scatter parameters with experimental measurements and to follow their variation, the Intralipid concentration was varied in the liquid phantom solution containing 1% blood, from 0.75% to 1.5% in steps of 0.25% (the data from 1% Intralipid was also used for Fig. 2). The amplitude and phase measurements were taken for each concentration, and the spectrally constrained reconstruction was applied to the data. The total hemoglobin was constant through the varying concentrations of Intralipid, and the saturation for both water and oxygen was 100% for all data sets. The mean value along with standard deviation from the images are plotted for scatter amplitude and scatter power in Fig. 3(a), and Fig. 3(b) shows the average  $\mu_s'$  at 661 and 785 nm. Figure 3(c) shows the total hemoglobin and Fig. 3(d) shows the oxygen saturation and water content. The scatter amplitude varies linearly with concentration and shows more variation (range 0.6–1.25) than the scatter power (range 1.3–1.53). Scatter power values are



(a)



(b)

Fig. 2. Recovered mean values with standard deviation error bars are shown in (a) from reconstructed data with a 90-mm-diameter liquid phantom containing 1% Intralipid with 9.3- $\mu\text{M}$  total hemoglobin. Values for the spectrally constrained reconstruction are shown alongside those obtained with the conventional reconstruction approach and the true theoretical values. (b) Images from this phantom are shown for comparison with the spectrally constrained reconstruction (top row), the conventional reconstruction (middle row), and the profile plots from the midplane of these images (bottom row).

comparable with the expected value of 1.4 from van Staveren *et al.*,<sup>19</sup> showing a mean of  $1.4 \pm 0.1$  through the change in concentrations. The mean  $\mu_s'$  at 785 nm varies linearly (slope of  $\approx 1$ ) with the change in percent Intralipid, and the value approximately doubles (0.89 versus  $1.7 \text{ mm}^{-1}$ ) when the concentration doubles from 0.75% to 1.5% Intralipid, which is encouraging. The reduced scattering coefficient at 661 nm also shows a similar trend. The total hemoglobin stays constant with change in scattering

with a mean of  $8.2 \mu\text{M} \pm 0.8$ , and the oxygen saturation shows a mean value of  $99.3\% \pm 1.2\%$ , close to expected value of 100%. Water shows an average of  $92.4\% \pm 4.2\%$ , and some cross talk can be seen between hemoglobin and water at the higher Intralipid concentrations owing to the high-scattering medium.

#### D. Oxygen Saturation Validation

Malignant tumors typically have lower partial pressure values for oxygen ( $PO_2$ ) owing to hypoxia,<sup>26</sup> and

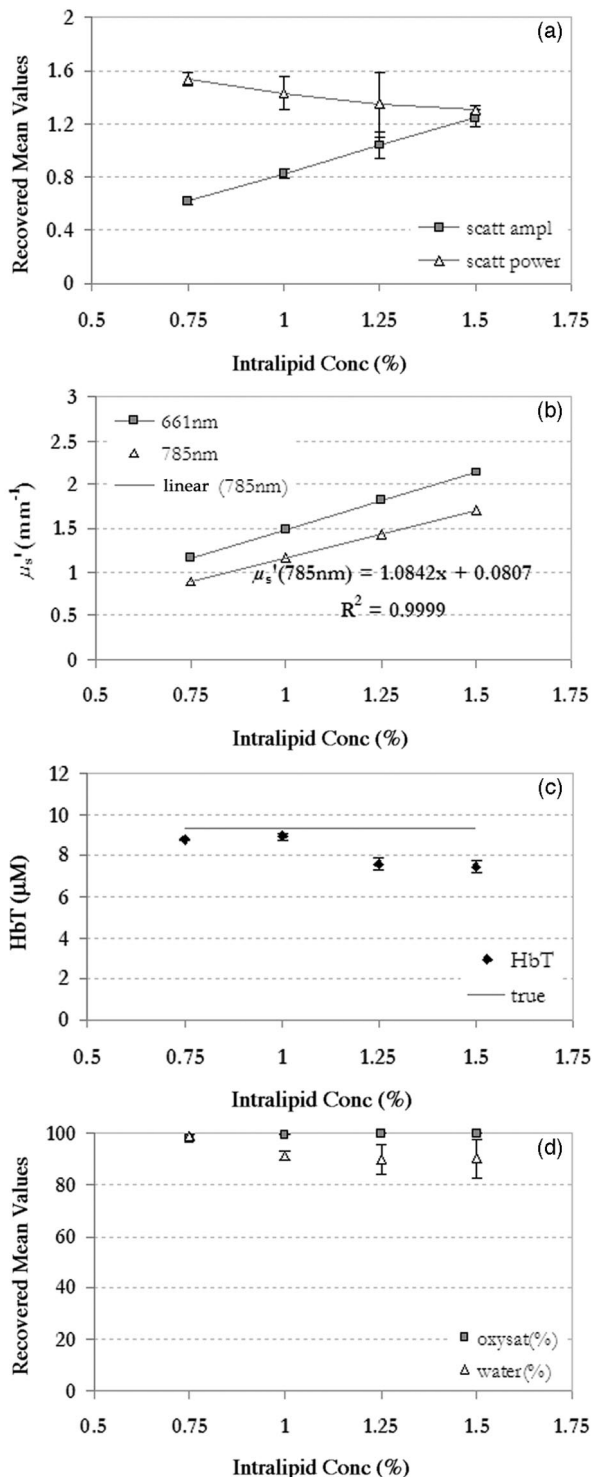


Fig. 3. Recovered mean values are shown from a series of phantoms in which the scattering coefficient was systematically varied through concentrations (Conc) of Intralipid ranging between 0.75% and 1.5%. The estimated scattering power and amplitudes are shown in (a), and the reduced scattering coefficients at 661 and 785 nm are shown in (b). The total hemoglobin, which did not vary, is shown in (c), along with a line corresponding to the theoretical value. In (d) the oxygen saturation and water values are shown, which also did not vary. Both have theoretical estimates of 100%. Error bars represent the standard deviation of all pixels within the interior 60 mm of the region imaged.

it is useful to verify that the spectrally constrained reconstruction can follow these hypoxic conditions. The relation between oxygen saturation and the variation in partial pressure of oxygen has a well-characterized behavior given by the Hill curve. This curve was obtained previously for the conventional method and published in Ref. 27. Data were acquired by use of a phantom solution containing 1% whole blood and 1% Intralipid in saline, in a thin-walled plastic container, 70-mm in diameter. The whole blood (1%) was found to have 18- $\mu\text{M}$  hemoglobin, and the oxygenation of the solution was reduced by varying the  $PO_2$  values from 150 to 0 mm Hg by the addition of yeast. The  $PO_2$  was independently measured by means of a chemical microelectrode after calibration of the electrode overnight in a saline solution. By varying the  $PO_2$  gradually, using a small amount of yeast, and making measurements over this period of time, we eventually reduced the  $PO_2$  to zero and obtained a complete set of data over the required range. The spectral reconstruction of this data gave HbT,  $SO_2$ , water, scatter amplitude, and scatter power images, from which the mean and standard deviation are plotted in Fig. 4. The oxygen saturation in Fig. 4(a) follows the theoretical Hill curve<sup>28</sup> reasonably well with a mean error of 7.7%, with the worst accuracy close to zero  $PO_2$  and the higher accuracy when  $PO_2$  is above 80% saturation. For  $PO_2$  below 20-mm Hg, oxygen saturation is still accurate to within 15%, with a low standard deviation in the images.

With variation of  $PO_2$ , the total hemoglobin concentration stayed approximately constant [Fig. 4(b)], with a mean value of  $17.5 \pm 2.1 \mu\text{M}$ , which is within 97% of the true value given above, and water exhibited a mean value of  $94.2\% \pm 8.3\%$ . Both parameters show some cross talk at  $PO_2$  values below 11-mm, which is possibly unavoidable owing to the limited number of wavelengths used in these data. Both scatter amplitude and scatter power stay approximately constant until a  $PO_2$  of 11-mm Hg, beyond which both show some variation, which could be the result of cross talk between the two parameters. Above 11-mm Hg, the scatter amplitude has value of  $0.92 \pm 0.04 \cdot 10^{-3b}(\text{mm})^{b-1}$ , and the scatter power has values of  $1.49 \pm 0.14$ . The reduced scattering coefficient, however, stays constant throughout, as shown for 785 nm in Fig. 4(d), with a mean of  $1.3 \pm 0.03 \text{ mm}^{-1}$ .

#### E. Total Hemoglobin Validation

The final experimental homogeneous data set involved varying the total hemoglobin while keeping oxygen saturation, water, and scatter parameters constant. This was accomplished by use of a similar liquid phantom, with 1% Intralipid in saline, and by variation of the concentration of whole blood. The hematocrit level was measured by a clinical co-oximeter, yielding 1% blood, which is equivalent to 22- $\mu\text{M}$  total hemoglobin. The blood concentration was varied from 0.2% to 1% in increments of 0.2%, and the amplitude and phase

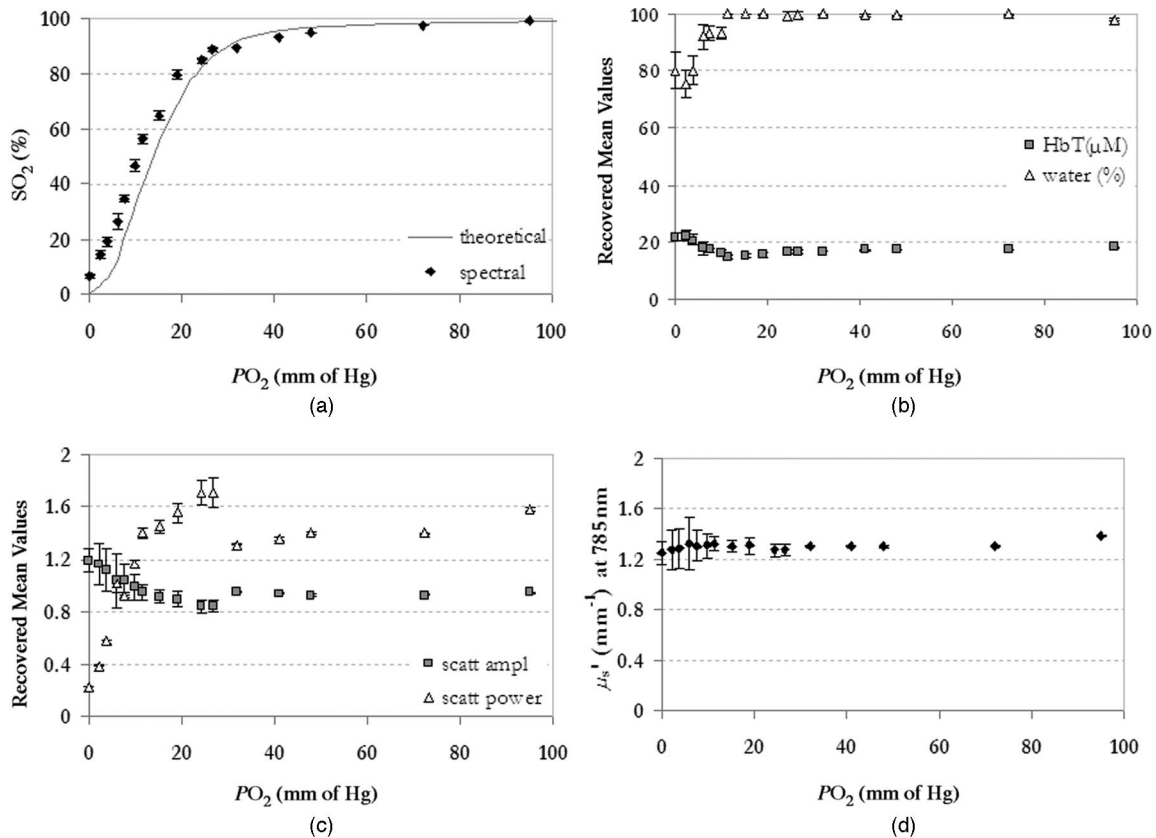


Fig. 4. Estimated mean values are shown from homogeneous reconstructions of a phantom with varying oxygen partial pressure ( $PO_2$ ) of the solution induced by addition of yeast. The oxygen saturation is shown in (a), along with the theoretical estimate from the Hill curve. The total hemoglobin and percent water are shown in (b) with the theoretically estimated values of 18 mM and 100%, respectively, and should not vary with changes in oxygenation. The scatter power and amplitude are shown in (c) and should not vary. The reduced scattering coefficient at 785 nm is also shown in (d).

measurements were obtained for each level. After calibration, the spectrally constrained reconstruction was applied to the data, and the recovered mean and standard deviation from the NIR parameters are plotted in Fig. 5. The theoretical water and oxygen saturation values were 100%, as the phantom was a liquid oxygenated solution.

Figure 5(a) shows that the total hemoglobin followed the variation in blood (%) linearly and is quantitatively accurate, with a mean percent error of 6.2%. Oxygen saturation stayed constant with change in blood concentration [Fig. 5(b)], with a mean value of  $98.9 \pm 0.6\%$ . The same trend was found in water, with a mean value of  $98.2\% \pm 1.5\%$ . The scatter amplitude and scatter power, shown in Fig. 5(b), are also independent of the variation in blood concentration, with a scatter amplitude of  $0.65 \pm 0.01$ . The scatter power had a mean value of  $1.39 \pm 0.08$ , and this agreed well with the estimated 1.4 derived from van Staveren *et al.*<sup>19</sup> The reconstruction converged in 4–6 iterations for the different concentrations, and no spatial filtering was applied in the reconstruction.

#### 4. Discussion and Conclusions

The spectrally constrained direct chromophore and scattering reconstruction has been implemented and

validated by use of simulated and experimental frequency-domain measurements. The results from Subsection 3.A show improved robustness of the reconstruction to increased amounts of noise in the data. The frequency-domain instrumentation in use typically has 0.5% noise in amplitude and 0.5 deg in phase,<sup>11</sup> and at this noise level. With simulated data from a homogeneous phantom, water images show a reduction in standard deviation from 32% to 10% (as percent of the mean) in going from the conventional to the spectral approach. Even at a 5% noise level, the spectral approach shows recovery of the parameters that is accurate within 10%, on average, with a significantly reduced standard deviation as compared with the conventional method. This insensitivity to noise is due to the use of multiwavelength data together with the spectral constraints, which results in a reduction in the number of unknowns, making the reconstruction problem less ill posed. The reduction in noise in the images is also observed in the homogeneous experimental data and is especially significant in water and scatter power. The NIR parameter images in Fig. 2 show the suppression of the artifacts in the images, particularly in water and scatter power, that is similar to the trend observed in the simulated data.

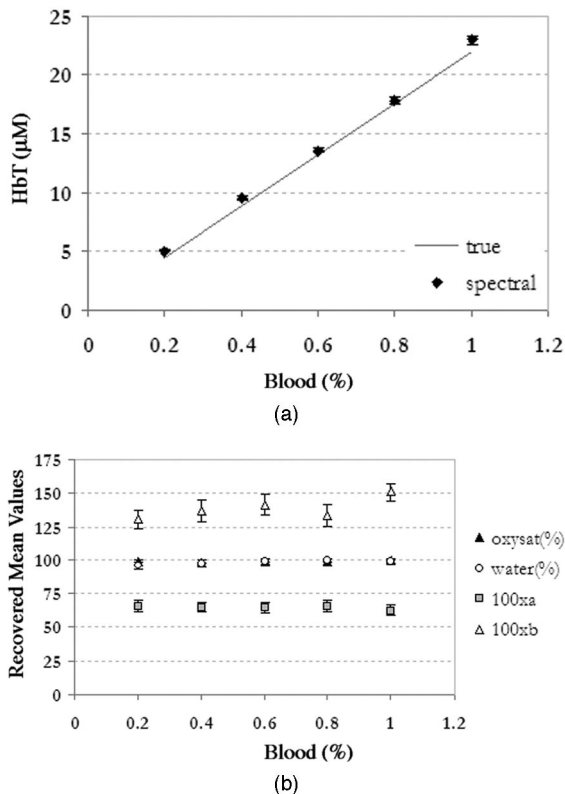


Fig. 5. Reconstructed mean and standard deviation values are shown from phantoms with varying concentrations of blood in which the total hemoglobin is graphed (a) alongside the theoretical value shown by a dotted line. The recovered values of oxygen saturation (%), water (%), scattering amplitude (a) and scattering power (b) are shown in (b), all of which are not expected to vary with changes in total blood (%). The scatter parameters are multiplied by 100 to allow them to be displayed on the same graph as the oxygen saturation and the water.

Water is an important measure of breast physiology; however, its quantitative accuracy from NIR tomography has yet to be validated. In the past several studies used a fixed water content in tissue (such as assuming 30%–31% fraction in tissue) to allow for spectral fitting of hemoglobin levels<sup>29,30</sup> or used radiological data<sup>31</sup> because sufficient wavelengths were unavailable and the cross talk between water and oxyhemoglobin prevented quantitatively accurate recovery of the water absorption. McBride *et al.*<sup>32</sup> and Cerussi *et al.*<sup>33</sup> have shown that using sparse spectral image data from a subject with assumptions about the bulk concentration for water and lipids could have up to 15% influence on HbT and oxygen saturation estimates. In recent studies water has been shown to have significant variation with breast size in normal subject studies,<sup>24</sup> with values between subjects varying significantly from 10% to 70%. This large range was observed in a 30-subject population, as shown by Cerussi *et al.*,<sup>33</sup> and values of 21% to 82% were observed in a 26-subject population studied by Srinivasan *et al.*<sup>24</sup> These large numbers suggest that water is a measure of the extravascular space, since the vascular space is clearly less than 2% in most

breast tissues. Thus water yields different information about the physiology of the breast than does hemoglobin, and spatial changes are expected in water owing to different content in the fatty and glandular tissues, which varies with the composition of the breast. The change in water content during the course of the menstrual cycle has been followed by Cubeddu *et al.*, showing an increase in water in the second half of the cycle<sup>34</sup> for one patient. Shah *et al.*<sup>35</sup> have shown an increase of up to 28.1% in water in the luteal phase in a single volunteer, and Pogue *et al.*<sup>36</sup> have shown individual variations in seven subjects, with a mean value nearer to 2.5%. In a study following the effect of neoadjuvant chemotherapy<sup>37</sup> in a subject with a palpable adenocarcinoma, using optical white-light spectroscopy, water showed the most dramatic change, dropping 67% over the course of three treatment cycles. These studies have shown important trends in water content. However, to improve the clinical utility of the recovered values, it is important to show that they are quantitatively accurate estimates as well. The results shown here provide evidence of improvement in the quantification of water by use of the spectrally constrained approach compared with the conventional method of fitting for the chromophore and scattering parameters from optical property reconstructions. Water fraction values obtained by the new approach in data sets that follow variation in scattering, oxygen saturation, and total hemoglobin agree well with theoretical predictions and exhibit reduced noise and cross talk with oxyhemoglobin compared with the conventional technique.

Scattering is another area in which the constraints from Mie theory incorporated into the reconstruction significantly improve the quantification of the scatter amplitude and power. Recent studies have used scattering to study structural variations. For example, Poplack *et al.*<sup>38</sup> showed in a normal cohort of 23 women that there is a significant decrease in the reduced scattering coefficient ( $\mu_s'$ ) at 785 nm with increasing body mass index and that adipose tissue was less scattering than glandular tissue, as expected. The same trend was observed by Durduran *et al.*<sup>29</sup> in a subject pool of 52 volunteers. Cerussi *et al.*<sup>33</sup> used the fit of  $\mu_s'$  to the Mie theory approximation to show that scatter power decreases with increasing body mass index in a group of 30 healthy women. Pogue *et al.*<sup>36</sup> showed that scattering power and scatter amplitude could successfully separate categories of fatty and scattered breasts from extremely dense breasts ( $p < 10^{-4}$ ) in a survey of 39 women with normal mammography. Since the risk of cancer is strongly correlated to the breast density,<sup>39</sup> this separation of breast densities in a noninvasive manner could prove very useful. Although these trends may prove to be promising in the future, their quantitative accuracy must be validated in phantom studies. Hence it is important to investigate the accuracy and standard deviation in these parameters to fully exploit the NIR information. Results in Subsection 3.A show the improved reconstruction of scatter power

images with robustness maintained at noise levels as high as 5% noise. In Fig. 2 the recovered mean for the scatter amplitude and scatter power agree well with predicted values from van Steveran *et al.*<sup>19</sup> for homogeneous experimental data (containing 1% blood and 1% Intralipid in saline). A change in scattering, obtained by varying the Intralipid concentration in a homogeneous phantom solution, was successfully followed (Fig. 3), in which the scatter amplitude varied linearly and the scatter power showed a mean of  $1.4 \pm 0.1$  during the changes in concentration. The cross talk between scatter parameters and chromophore concentrations is minimal, with total hemoglobin, oxygen saturation, and water content staying constant through this change [Figs. 3(c) and 3(d)], except at the highest scattering concentration of Intralipid (1.5%). The mean of  $\mu_s'$  also exhibits a linear increase, and  $\mu_s'$  at 785 nm doubles as the Intralipid concentration changes from 0.75% ( $\mu_s' = 0.89 \text{ mm}^{-1}$ ) to 1.5% ( $\mu_s' = 1.7 \text{ mm}^{-1}$ ), shown in Fig. 3(b).

The Hill curve relation between oxygen saturation ( $\text{SO}_2$ ) and  $\text{PO}_2$  of oxygen was followed by the spectral method in the graphs of Fig. 4, which showed that  $\text{SO}_2$  was accurate, with a mean error of 7.7%. Total hemoglobin estimates remained constant through this change in  $\text{PO}_2$ , producing a mean that is accurate to 97% of the expected value. Water content also showed this trend, with a mean of 94.2%, which compared well with the predicted value of 100%. Although some variation was found in the scatter amplitude and scatter power,  $\mu_s'$  at 785 nm remained constant with change in oxygenation, with a mean of  $1.3 \pm 0.03 \text{ mm}^{-1}$ . The standard deviations in the oxygen saturation images remain low, even at lower oxygenation. This translates into a successful recovery of  $\text{SO}_2$  in malignancies without significant noise or cross talk between scatter parameters and deoxyhemoglobin. Total hemoglobin recovered by the spectral approach was separately validated by use of experimental data obtained by varying blood concentration from 0.2% to 1%. Quantitatively accurate results with a mean percent error of 6.2% were obtained. No cross talk between any of the parameters was observed during this variation, as shown in Fig. 5(b) in which oxygen saturation, water, scatter amplitude, and scatter power remained unchanged and close to predicted values.

The spectrally constrained approach is inherently robust owing to the addition of *a priori* spectral behavior. It requires less spatial filtering, whereas the conventional technique benefits from a mean filter to prevent excessive noise in the images. This new approach also converges faster and is readily extendable to three-dimensional models as well. Use of data at additional wavelengths can easily be implemented without much computational burden in the inversion process. A partial volume-type reconstruction may be an efficient means of processing a large number of measurements. There is certainly some cross talk found at  $\text{PO}_2$  values of oxygen lower than 11-mm Hg

or under extremely high scattering conditions, which can probably be resolved only by the addition of more wavelengths. Preliminary simulations have shown this to be true. The improved quantification of and robustness to noise of the reconstruction shown here for homogeneous measurements is currently also apparent in the heterogeneous data.

As the use of NIR tomography expands, spectrally constrained reconstruction should add considerable value to obtaining quantitatively accurate estimates of different parameters, particularly water and scatter power. The use of frequency-domain measurements allows a good separation of chromophore and scattering, and together with the spectral approach, we obtain reduced cross talk between the parameters, suppression of image artifacts, insensitivity to noise in the measurements, and, finally, accurate quantification of the NIR parameters.

This study was supported through National Institutes of Health grants PO1CA80139 and RO1CA69544 and through the Department of Defense grant DAMD17-03-01-0405.

## References

1. B. W. Pogue, S. P. Poplack, T. O. McBride, W. A. Wells, O. K. S. Osterman, U. L. Osterberg, and K. D. Paulsen, "Quantitative hemoglobin tomography with diffuse near-infrared spectroscopy: pilot results in the breast," *Radiology* **218**, 261–266 (2001).
2. B. J. Tromberg, N. Shah, R. Lanning, A. Cerussi, J. Espinoza, T. Pham, L. Svaasand, and J. Butler, "Non-invasive *in vivo* characterization of breast tumors using photon migration spectroscopy," *Neoplasia (New York)* **2**, 26–40 (2000).
3. D. Grosznick, H. Wabnitz, K. T. Moesta, J. Mucke, M. Moller, C. Stroszczynski, J. Stossel, B. Wassermann, P. M. Schlag, and H. Rinneberg, "Concentration and oxygen saturation of hemoglobin of 50 breast tumors determined by time-domain optical mammography," *Phys. Med. Biol.* **49**, 1165–1181 (2004).
4. A. Corlu, T. Durduran, R. Choe, M. Schweiger, E. M. Hillman, S. R. Arridge, and A. G. Yodh, "Uniqueness and wavelength optimization in continuous-wave multispectral diffuse optical tomography," *Opt. Lett.* **28**, 2339–2341 (2003).
5. A. Li, Q. Zhang, J. P. Culver, E. L. Miller, and D. A. Boas, "Reconstructing chromosphere concentration images directly by continuous-wave diffuse optical tomography," *Opt. Lett.* **29**, 256–258 (2004).
6. S. R. Arridge and M. Schweiger, "Image reconstruction in optical tomography," *Philos. Trans. R. Soc. London Ser. B* **352**, 717–726 (1997).
7. K. D. Paulsen and H. Jiang, "Spatially varying optical property reconstruction using a finite element diffusion equation approximation," *Med. Phys.* **22**, 691–701 (1995).
8. M. S. Patterson, B. C. Wilson, and D. R. Wyman, "The propagation of optical radiation in tissue I. Models of radiation transport and their application," *Lasers Med. Sci.* **6**, 155–168 (1990).
9. B. Brandstatter, K. Hollaus, H. Hutten, M. Mayer, R. Merwa, and H. Scharfetter, "Direct estimation of Cole parameters in multifrequency EIT using a regularized Gauss–Newton method," *Physiol. Meas.* **24**, 437–448 (2003).
10. Q. Fang, P. M. Meaney, S. D. Geimer, A. V. Streltsov, and K. D. Paulsen, "Microwave image reconstruction from 3-D fields coupled to 2-D parameter estimation," *IEEE Trans. Med. Imaging* **23**, 475–484 (2004).
11. T. O. McBride, B. W. Pogue, S. Jiang, U. L. Osterberg, and K. D. Paulsen, "A parallel-detection frequency-domain near-

- infrared tomography system for hemoglobin imaging of the breast *in vivo*,” *Rev. Sci. Instrum.* **72**, 1817–1824 (2001).
12. T. O. McBride, B. W. Pogue, U. L. Osterberg, and K. D. Paulsen, “Strategies for absolute calibration of near infrared tomographic tissue imaging,” in *Oxygen Transport to Tissue XXI*, J. F. Dunn and H. M. Swartz, eds., (Pabst, Lengerich, Germany, 2001).
  13. A. Ishimaru, *Wave Propagation and Scattering in Random Media*, Vol. 1 (Academic, New York, 1978).
  14. H. Jiang, K. D. Paulsen, U. L. Osterberg, B. W. Pogue, and M. S. Patterson, “Optical image reconstruction using frequency-domain data: simulations and experiments,” *J. Opt. Soc. Am. A* **13**, 253–266 (1996).
  15. H. Dehghani, B. W. Pogue, J. Shudong, B. Brooksby, and K. D. Paulsen, “Three-dimensional optical-tomography: resolution in small-object imaging,” *Appl. Opt.* **42**, 3117–3128 (2003).
  16. D. W. Marquardt, “An algorithm for least squares estimation of nonlinear parameters,” *J. Soc. Ind. Appl. Math.* **11**, 431–441 (1963).
  17. W. H. Press, S. A. Teukolsky, W. J. Vetterling, and B. P. Flannery, *Numerical Recipes in Fortran: the Art of Scientific Computing*, 2nd ed. (Cambridge U. Press, Cambridge, UK, 1986).
  18. T. O. McBride, B. W. Pogue, E. Gerety, S. Poplack, U. L. Osterberg, and K. D. Paulsen, “Spectroscopic diffuse optical tomography for quantitatively assessing hemoglobin concentration and oxygenation in tissue,” *Appl. Opt.* **38**, 5480–5490 (1999).
  19. H. J. van Staveren, C. J. M. Moes, J. van Marle, S. A. Prahl, and J. C. van Gemert, “Light scattering in Intralipid-10% in the wavelength range of 400–1100 nm,” *Appl. Opt.* **30**, 4507–4514 (1991).
  20. J. R. Mourant, T. Fuselier, J. Boyer, T. M. Johnson, and I. J. Bigio, “Predictions and measurements of scattering and absorption over broad wavelength ranges in tissue phantoms,” *Appl. Opt.* **36**, 949–957 (1997).
  21. J. M. Steinke and A. P. Shepherd, “Comparison of Mie theory and the light scattering of red blood cells,” *Appl. Opt.* **27**, 4027–4033 (1988).
  22. B. Beauvoit, H. Liu, K. Kang, P. D. Kaplan, M. Miwa, and B. Chance, “Characterization of absorption and scattering properties for various yeast strains by time-resolved spectroscopy,” *Cell Biophys.* **23**, 91–109 (1993).
  23. K. D. Paulsen, P. M. Meaney, M. J. Moskowitz, and J. M. Sullivan, “A dual mesh scheme for finite element based reconstruction algorithms,” *IEEE Trans. Med. Imaging* **14**, 504–514 (1995).
  24. S. Srinivasan, B. W. Pogue, S. Jiang, H. Dehghani, C. Kogel, S. Soho, J. J. Gibson, T. D. Tosteson, S. P. Poplack, and K. D. Paulsen, “Interpreting hemoglobin and water concentration, oxygen saturation and scattering measured *in vivo* by near-infrared breast tomography,” *Proc. Natl. Acad. Sci. USA* **100**, 12349–12354 (2003).
  25. X. Song, B. W. Pogue, T. D. Tosteson, T. O. McBride, S. Jiang, and K. D. Paulsen, “Statistical analysis of nonlinearly reconstructed near-infrared tomographic images: Part II—Experimental interpretation,” *IEEE Trans. Med. Imaging* **21**, 764–772 (2002).
  26. P. Vaupel, F. Kallinowski, and P. Okunieff, “Blood flow, oxygen and nutrient supply, and metabolic microenvironment of human tumors: a review,” *Cancer Res.* **49**, 6449–6465 (1989).
  27. S. Srinivasan, B. W. Pogue, S. Jiang, H. Dehghani, and K. D. Paulsen, “Validation of hemoglobin and water molar absorption spectra in near-infrared diffuse optical tomography,” in *Optical Tomography and Spectroscopy of Tissue V*, B. Chance, R. R. Alfano, B. J. Tromberg, M. Tamura, and E. M. Sevick-Muraca, eds., *Proc. SPIE* **4955**, 407–415 (2003).
  28. N. Varjavand, “The interactive oxyhemoglobin dissociation curve,” <http://www.ventworld.com/resources/oxydisso/dissohtml.2002>.
  29. T. Durduran, R. Choe, J. P. Culver, L. Zubkov, M. J. Holboke, J. Giammarco, B. Chance, and A. G. Yodh, “Bulk optical properties of healthy female breast tissue,” *Phys. Med. Biol.* **47**, 2847–2861 (2002).
  30. D. Grosenick, K. T. Moesta, H. Wabnitz, J. Mucke, C. Stroszczynski, R. Macdonald, P. M. Schlag, and H. Rinneberg, “Time-domain optical mammography: initial clinical results on detection and characterization of breast tumors,” *Appl. Opt.* **42**, 3170–3186 (2003).
  31. D. R. White and H. Q. Woodard, “Average soft-tissue and bone models for use in radiation dosimetry,” *Br. J. Radiol.* **60**, 907–913 (1987).
  32. T. O. McBride, B. W. Pogue, S. Jiang, U. L. Osterberg, K. D. Paulsen, and S. P. Poplack, “Multi-spectral near-infrared tomography: a case study in compensating for water and lipid content in hemoglobin imaging of the breast,” *J. Biomed. Opt.* **7**, 72–79 (2002).
  33. A. Cerussi, D. Jakubowski, N. Shah, F. Bevilacqua, R. Lanning, A. J. Berger, D. Hsiang, J. Butler, R. F. Holcombe, and B. J. Tromberg, “Spectroscopy enhances the information content of optical mammography,” *J. Biomed. Opt.* **7**, 60–71 (2002).
  34. R. Cubeddu, C. D’Andrea, A. Pifferi, P. Taroni, A. Torricelli, and G. Valentini, “Effects of the menstrual cycle on the red and near-infrared optical properties of the human breast,” *Photochem. Photobiol.* **72**, 383–391 (2000).
  35. N. Shah, A. Cerussi, C. Eker, J. Espinoza, J. Butler, J. Fishkin, R. Hornung, and B. Tromberg, “Noninvasive functional optical spectroscopy of human breast tissue,” *Proc. Natl. Acad. Sci. USA* **98**, 4420–4425 (2001).
  36. B. W. Pogue, S. Jiang, H. Dehghani, C. Kogel, S. Soho, S. Srinivasan, X. Song, S. P. Poplack, and K. D. Paulsen, “Characterization of hemoglobin, water and NIR scattering in breast tissue: analysis of inter-subject variability and menstrual cycle changes relative to lesions,” *J. Biomed. Opt.* **9**, 541–552 (2004).
  37. D. B. Jakubowski, A. E. Cerussi, F. Bevilacqua, N. Shah, D. Hsiang, J. Butler, and B. J. Tromberg, “Monitoring neoadjuvant chemotherapy in breast cancer using quantitative diffuse optical spectroscopy: a case study,” *J. Biomed. Opt.* **9**, 230–238 (2004).
  38. S. P. Poplack, K. D. Paulsen, A. Hartov, P. M. Meaney, B. W. Pogue, T. D. Tosteson, M. R. Grove, S. K. Soho, and W. A. Wells, “Electromagnetic breast imaging: average tissue property values in women with negative clinical findings,” *Radiology* **231**, 571–580 (2004).
  39. M. T. Mandelson, N. Oestreicher, P. L. Porter, D. White, C. A. Finder, S. H. Taplin, and E. White, “Breast density as a predictor of mammographic detection: comparison of interval- and screen-detected cancers,” *J. Natl. Cancer Inst.* **92**, 1081–1087 (2000).